communications physics

ARTICLE

https://doi.org/10.1038/s42005-021-00621-4 OPEN

Magnetic and *f*-electron effects in $LaNiO_2$ and $NdNiO_2$ nickelates with cuprate-like $3d_{x^2-y^2}$ band

Ruiqi Zhang[1✉], Christopher Lane[2,3], Bahadur Singh[4], Johannes Nokelainen[5,6], Bernardo Barbiellini[5,6], Robert S. Markiewicz[6], Arun Bansil[6✉] & Jianwei Sun[1✉]

Recent discovery of superconductivity in the doped infinite-layer nickelates has renewed interest in understanding the nature of high-temperature superconductivity more generally. The low-energy electronic structure of the parent compound $NdNiO_2$, the role of electronic correlations in driving superconductivity, and the possible relationship between the cuprates and the nickelates are still open questions. Here, by comparing $LaNiO_2$ and $NdNiO_2$ systematically within a parameter-free, all-electron first-principles density-functional theory framework, we reveal the role of Nd 4*f* electrons in shaping the ground state of pristine $NdNiO_2$. Strong similarities are found between the electronic structures of $LaNiO_2$ and $NdNiO_2$, except for the effects of the 4*f* electrons. Hybridization between the Nd 4*f* and Ni 3*d* orbitals is shown to significantly modify the Fermi surfaces of various magnetic states. In contrast, the competition between the magnetically ordered phases depends mainly on the gaps in the Ni $3d_{x^2-y^2}$ band. Our estimated value of the on-site Hubbard *U* in the nickelates is similar to that in the cuprates, but the value of the Hund's coupling J_H is found to be sensitive to the Nd magnetic moment. In contrast with the cuprates, $NdNiO_2$ presents 3D magnetism with competing antiferromagnetic and (interlayer) ferromagnetic exchange, which may explain why the T_c is lower in the nickelates.

[1] Department of Physics and Engineering Physics, Tulane University, New Orleans, LA, USA. [2] Theoretical Division, Los Alamos National Laboratory, Los Alamos, NM, USA. [3] Center for Integrated Nanotechnologies, Los Alamos National Laboratory, Los Alamos, NM, USA. [4] Department of Condensed Matter Physics and Materials Science, Tata Institute of Fundamental Research, Mumbai, India. [5] Department of Physics, School of Engineering Science, LUT University, Lappeenranta, Finland. [6] Department of Physics, Northeastern University, Boston, MA, USA. ✉email: rzhang16@tulane.edu; ar.bansil@neu.edu; jsun@tulane.edu

Since the discovery of high-T_c superconductivity (HTSC) in the lanthanum-based cuprates in 1986[1], understanding the mechanism of HTSC has drawn intense interest[2–6]. Despite vigorous efforts, however, many questions remain unanswered and a clear consensus on the underlying mechanism of HTSC has remained elusive. A promising route in this connection is to find superconducting analogs of the cuprates, which could provide new clues to the origin of HTSC. One such materials family is the perovskite nickel oxides. Here the infinite-layer $NdNiO_2$ compound holds great promise since it exhibits an intrinsic $3d^9$ filling much like the cuprates, although challenges of crystal growth have presented problems for undertaking systematic investigations.

Superconductivity in the hole-doped infinite-layer nickelate $NdNiO_2$ at 9–15K has been reported in thin-film samples grown on $SrTiO_3$[7–10], although superconductivity in bulk $NdNiO_2$ has not been observed[11]. These results[7] have reinvigorated interest in searching for the microscopic mechanism of HTSC and stimulated many new questions[10–20]. Notably, superconductivity is present both in the hole-doped $NdNiO_2$[7] and $PrNiO_2$[21], but it is absent in $LaNiO_2$[7]. This suggests that the Nd (Pr) *f*-electrons are not merely spectators, but possibly participate in the emergence of superconductivity. Interestingly, initial reports showed metallic behavior in pristine $LaNiO_2$ and $NdNiO_2$ with no sign of long-range magnetic order persisting down to low temperatures[11,22,23], calling into question the role of Mott physics in driving superconductivity. However, two recent transport studies[8,10] report the presence of a weak insulating phase in pristine $NdNiO_2$, which could partly be a signature of short-range magnetic fluctuations due to the intrinsic off-stoichiometry produced by the inhomogeneous oxygen deintercalation crystal-growth process[7].

In this connection, a variety of theoretical studies have been performed to understand the low-energy physics of the nickelates employing density functional theory (DFT)[14,18,24–26] and "beyond" DFT methods such as DFT+U[18,27,28], quasiparticle GW[29], dynamical mean-field theory (DMFT)[27,30–32], and model Hamiltonians[15,17,27,33] that have been constructed to understand the low-energy physics. The bulk of these studies focus on the NiO_2 plane and differences in quantities such as the $d-p$ orbital splitting in comparison to the cuprates[18]. However, focusing on the NiO_2 plane neglects the effects of the *f* electrons on the electronic and magnetic structure, despite the presence of superconductivity in the Nd-based and Pr-based compounds but not in the La compounds[7,21]. An active role of the *f* electrons is also suggested by a Kondo-like logarithmic temperature dependence of the resistivity and Hall coefficient at low temperatures[7], and other recent experiments demonstrating strong similarities between the infinite-layer nickelates and the rare-earth intermetallics[34], although a recent study attributes this strange behavior to the Nd 5*d* orbitals[15]. A few electronic structure studies utilizing the DFT+U[16] scheme or Heyd–Scuseria–Ernzerhof (HSE) hybrid functional[25] have considered the *f* electrons and found significant hybridization between the Nd 4*f* and Ni 3*d* orbitals near the chemical potential along with a possible ferromagnetic order. But, these calculations neglect the effects of spin–orbit coupling (SOC) crucial for capturing the correct *f*-band splittings, and required the introduction and fine tuning of external ad hoc parameters such as the Hubbard *U* and the exact-exchange admixture, limiting their predictive power[35].

In this article, we present a systematic in-depth study of the electronic and magnetic structures of both $LaNiO_2$ and $NdNiO_2$ using the strongly-constrained-and-appropriately-normed (SCAN) density functional[36] with spin–orbit coupling to examine the effects of *f* electron physics. The SCAN functional has proven accurate for modeling many correlated materials families including the cuprates[37–41], iridates[42], and the ABO_3 materials[43]. In particular, SCAN accurately predicts the *f*-band splitting in SmB_6 in good accord with the corresponding experimental values[44]. We consider a number of magnetic phases, whose energy and ordering are found to be quite similar for $LaNiO_2$ and $NdNiO_2$ with sensitivity to the opening of magnetic gaps in the Ni $3d_{x^2-y^2}$ band. The dispersion of this band is quite similar to that of the corresponding band in the cuprates, as is the order of the resulting magnetic phases where the antiferromagnetic state has the lowest energy. In line with this, the estimated values of the Hubbard *U* are close to those commonly found in the cuprates, while Hund's coupling J_H varies for different Nd magnetic sublattices. However, unlike the cuprates[37], the strength of the interlayer magnetic exchange coupling in the nickelates is comparable to that of the intralayer exchange with a strong antiferromagnetic component. Lastly, the 4*f* electrons play an important role in modifying the Fermi surfaces in the nickelates, where we find the charge transfer energy between the Ni 3*d* and O 2*p* orbitals to be large and do not change much with magnetic order, indicating that the physics of the nickelates is distinct from that of the cuprates.

Results and discussion

Crystal and magnetic structures. Figure 1 shows the crystal structure of $LaNiO_2$ and $NdNiO_2$ in the *P*4/*mmm* symmetry[22], where NiO_2 planes are sandwiched together with La or Nd spacer layers. In the NiO_2 planes the Ni sites are surrounded by four O atoms in square-planar coordination. The primitive cells for the non-magnetic (NM) and ferromagnetic (FM) phases are modeled by the primitive cell (Figs. 1a, b), respectively. Since unconventional superconductivity is often found accompanying an antiferromagnetic (AFM) phase transition, we also consider several AFM phases. In $NdNiO_2$, in particular, we find that the Nd and Ni sublattices can both support AFM spin orderings. Specifically, we use a $\sqrt{2}\times\sqrt{2}\times1$, $\sqrt{2}\times\sqrt{2}\times2$, and $1\times1\times2$ supercell for the *C*-type AFM (*C*-AFM), *G*-type AFM (*G*-AFM), and *A*-type AFM (*A*-AFM) orders, respectively, as shown in Figs. 1c–e. In the *C*-AFM phase, the intralayer coupling in both the Nd and Ni layers is AFM, whereas the interlayer coupling is FM. In the *G*-AFM phase both the intralayer and interlayer couplings are AFM. In contrast, the *A*-AFM phase displays an intralayer FM coupling with an AFM interlayer coupling for both the Nd and Ni sublattice.

Table 1 presents our theoretically predicted total energies, lattice constants, and spin magnetic moments for various magnetic phases of $LaNiO_2$ and $NdNiO_2$. For $LaNiO_2$, the *C*-AFM phase is the most stable, with the *G*-AFM, *A*-AFM, and NM phases lying at higher energies. The optimized lattice parameters for the magnetic phases are in good accord with the corresponding experimental values, while this is not the case for the lattice parameters obtained for the NM phase. Moreover, the lattice constant and the energy of the FM (*C*-AFM) phase are almost the same as that of the *A*-AFM (*G*-AFM) phase, indicating that the interlayer coupling in $LaNiO_2$ is very weak. Finally, our predicted local nickel magnetic moment is ~1.0 μ_B irrespective of the magnetic configuration.

Compared to our results, we note that GGA+U[18,45] ($U=3$) predicts a much smaller energy separation between the magnetic configurations along with reduced magnetic moments of ~0.7 μ_B and ~0.5 μ_B in the *C*-AFM and FM phases, respectively. The aforementioned reduced moments could be due to the neglect of SOC effects in the GGA+U calculations, but this is surprising since a significant Hubbard *U* was introduced on the Ni sites.

We now compare and contrast $LaNiO_2$ and $NdNiO_2$ with reference to Table 1. For both compounds, the *C*-AFM configuration is seen to be the most stable one. Energy of various

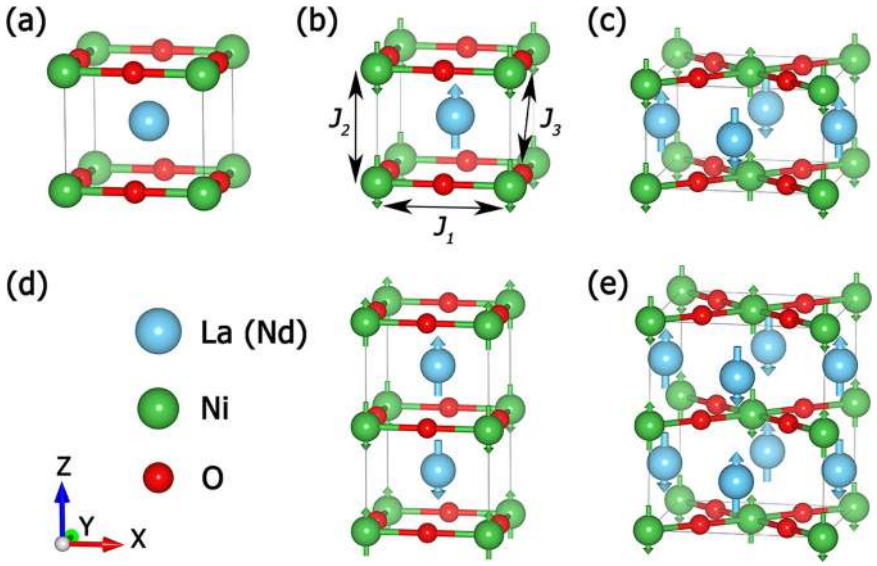

Fig. 1 Various crystal structures considered are shown. a Non-magnetic (NM), **b** ferromagnetic (FM). Three magnetic exchange couplings in the Ni sublattice are: J_1 (in-plane nearest-neighbor), J_2 (out-of-plane nearest-neighbor) and J_3 (out-of-plane next nearest-neighbor), **c** *C*-type antiferromagnetic (*C*-AFM), **d** *A*-type antiferromagnetic (*A*-AFM). **e** *G*-type antiferromagnetic (*G*-AFM) phase. The light blue, green, and red balls represent La (Nd), Ni, and O atoms, respectively. The light blue and green arrows denote different magnetic moment directions. Note that there is no local magnetic moment on La.

Table 1 Comparison of theoretically predicted properties of various magnetic phases of $LaNiO_2$ and $NdNiO_2$.

	$LaNiO_2$				
Phases	**Lattice constant (Å)**			**Energy**	M_{Ni}
	a	***b***	***c***	**(meV/f.u.)**	**(μB)**
NM	3.902	3.902	3.392	+400	0
C-AFM	3.949	3.949	3.346	0	1.05
G-AFM	3.947	3.947	3.345	+22	0.96
FM	3.943	3.943	3.366	+62	0.98
A-AFM	3.941	3.941	3.359	+64	1.00
Exp.[68]	3.959	3.959	3.375	-	-

	$NdNiO_2$					
Phases	**Lattice constant (Å)**			**Energy**	M_{Nd}	M_{Ni}
	a	***b***	***c***	**(meV/f.u)**	**(μB)**	**(μB)**
NM	3.836	3.836	3.177	+3792	0	0
C-AFM	3.910	3.910	3.239	0	2.91	1.05
G-AFM	3.901	3.901	3.239	+64	2.89	0.97
FM	3.904	3.904	3.302	+145	3.01	1.01
A-AFM	3.871	3.871	3.312	+155	2.98	0.96
Exp.[20]	3.914	3.914	3.239	-	-	-

Lattice constants refer to the primitive unit cell. Energies are given relative to the *C*-type antiferromagnetic phase. Values of magnetic moments display small variations among different Nd and Ni sites, the results given are the average values. M_{Nd} and M_{Ni} denote the local magnetic moment per Nd and Ni atom, respectively.

magnetic phases are greater in $NdNiO_2$ compared to the corresponding values in $LaNiO_2$. The NM phase lies at a high energy of 3840 meV/f.u. in $NdNiO_2$ and 400 meV/f.u. in $LaNiO_2$. These results suggest that $NdNiO_2$ has a stronger magnetic exchange coupling than $LaNiO_2$, a point to which we will return below. Also, we find the Ni–Nd coupling to be weakly AFM, and the Nd–Nd magnetic couplings to be small with a negligible effect on total energy, so that non-collinear magnetic orders could form in $NdNiO_2$ [see Supplementary Note 1]. Notably, like $LaNiO_2$, our calculated lattice constants for $NdNiO_2$ in the *C*-AFM and *G*-AFM phases are very close to the experimental values, while this is not the case for the values obtained in the NM, FM, and *A*-AFM arrangements.

Our computed local magnetic moments on Nd and Ni are seen from Table 1 to be ~3.0 μ_B and ~1.0 μ_B, respectively, suggesting that the corresponding electronic configurations of Nd and Ni are [Xe] $4f^3$ and $3d^9$. Various orbitals contribute to the total Ni magnetic moment as follows: 0.75 μ_B from $d_{x^2-y^2}$; 0.25 μ_B from d_{z^2}; and, t_{2g} carries a negligible moment. A number of theoretical studies in the literature have reported magnetic ordering and the associated local moments[16,28,45,46] with strong spin fluctuations possibly playing a key role in the pairing mechanism[32,46–48]. Specifically, the GGA yields the local moment on Ni to be significantly smaller with values of ~0.52 and ~0.35 μ_B in the FM and AFM phases, respectively[16]. [The SCAN values are only recovered when a large Hubbard U of 8(5) eV for Nd(Ni) is used[16].] A previous SCAN-based calculation[26] finds a reduced Ni magnetic moment of 0.76 μ_B, but this study neglected Nd 4*f* electrons and SOC effects. An LDA+U ($U = 6$ eV) calculation has predicted a Ni moment of 0.97 μ_B[49]. Lastly, the HSE06 hybrid functional yields moments of ~3.03 μ_B and ~0.89 μ_B on Nd and Ni sites, respectively, for the FM phase[25], similar to our SCAN values. Overall, our SCAN-based results are quite close to the expected *d* and *f* fillings of $NdNiO_2$ without invoking any ad hoc parameters such as *U*.

Regarding the presence of short-range magnetic order in the nickelates, strong spin-fluctuations, and AFM exchange interactions have been reported in $NdNiO_2$[50], and a quasi-static AFM order below 40 K has been reported in $Nd_{0.85}Sr_{0.15}NiO_2$[51]. Furthermore, related compounds, such as $LaNiO_3$[52] are AFM or are close to an AFM quantum critical point (QCP), suggesting that the nickelates with lower dimensions could also be close to magnetic order. Finally, DMFT calculations indicate the presence of strong spin fluctuations in the nickelates[32,48] with a fluctuating magnetic moment on Ni[32,48] of 1.1 μ_B, which is close to our value. Notably, although the DFT is expected to describe the ground state properties well[53–55], it is not expected to properly capture the spectral properties of correlated systems such as the self-energies.

Electronic structure of the NM phase. Figures 2a, b show the theoretically obtained band structures and densities of states

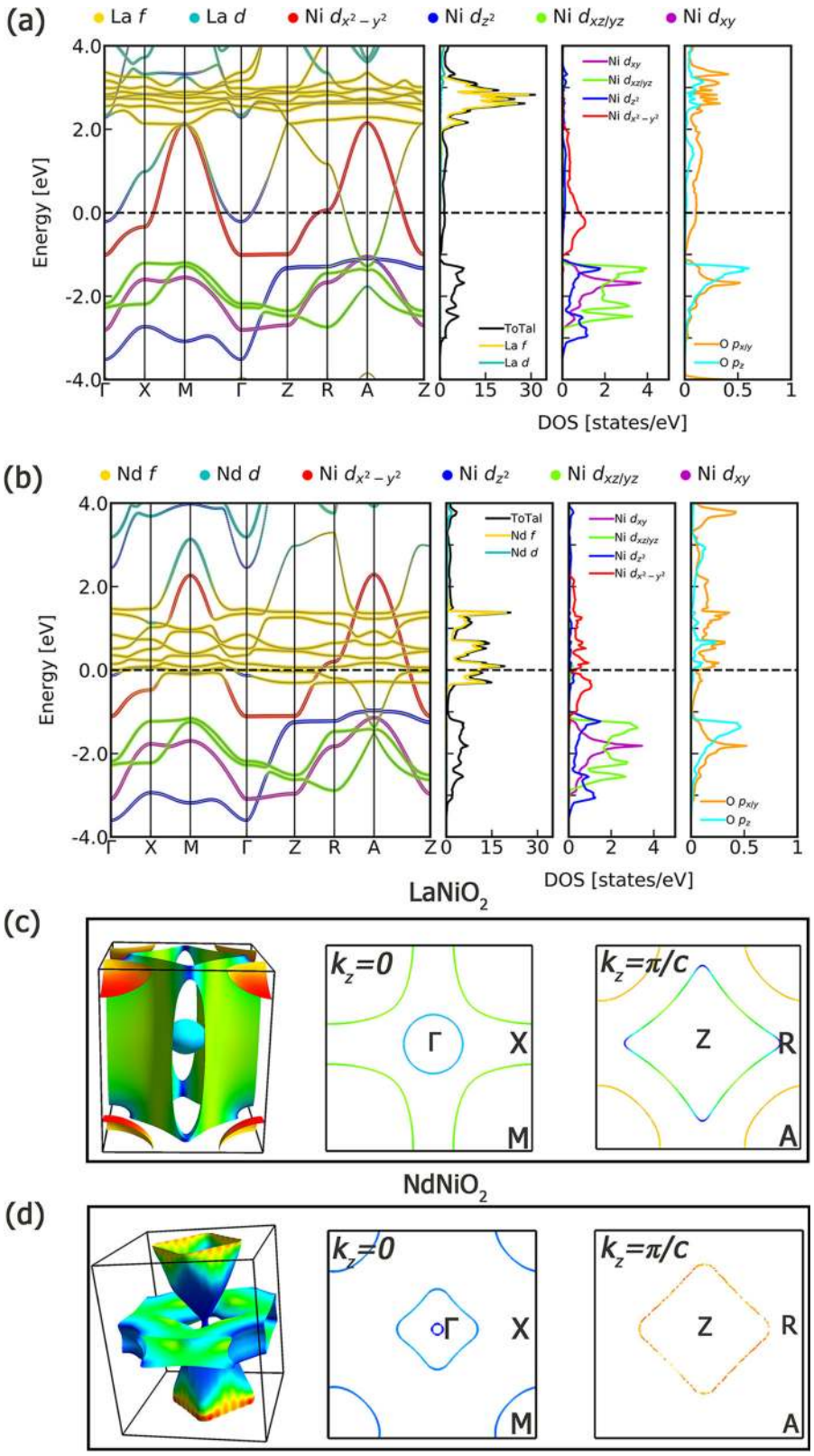

Fig. 2 The calculated electronic structures and Fermi surfaces of non-magnetic (NM) phase. Orbitally-projected electronic structures of NM phase of **a** $LaNiO_2$ and **b** $NdNiO_2$. **c** The calculated Fermi surface of $LaNiO_2$ and the projection of Fermi surface on $k_z = 0$ and π/c plane. **d** Same as **c** but for $NdNiO_2$. Red and blue colors identify portions of the Fermi surface where the Fermi velocity is maximum and minimum, respectively. The Fermi velocity lies in-between the maxima and minima in the green regions.

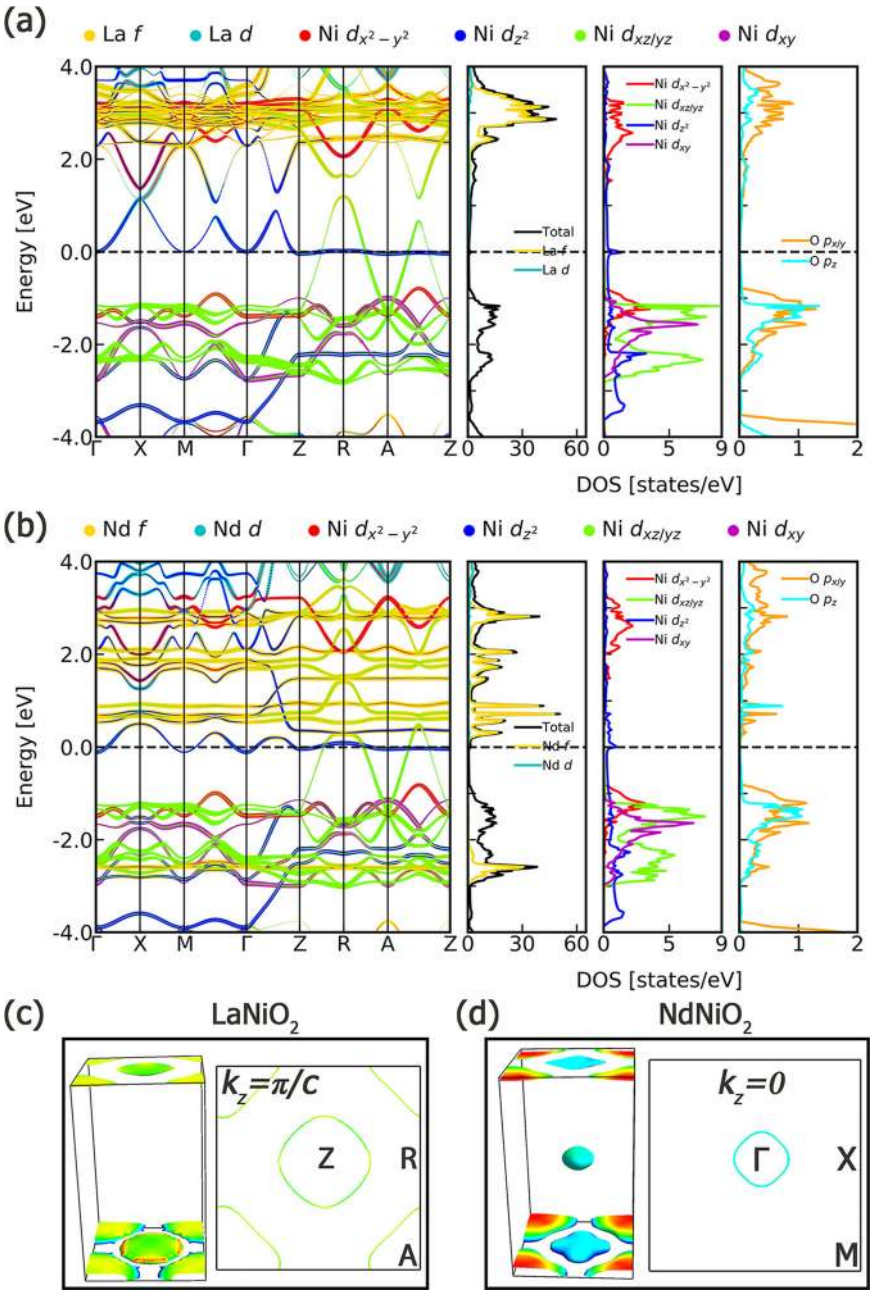

Fig. 3 The calculated electronic structures and Fermi surfaces of *C*-type antiferromagnetic (*C*-AFM) phase. Orbitally-projected electronic structures of *C*-type antiferromagnetic phase of **a** $LaNiO_2$ and **b** $NdNiO_2$. Band structures are "unfolded" on to the primitive $1 \times 1 \times 1$ Brillouin zone. **c** The calculated Fermi surface of $LaNiO_2$ and the projection of the Fermi surface on the $k_z = \pi/c$ plane. **d** Same as **c** but for $NdNiO_2$. Red and blue colors identify portions of the Fermi surface where the Fermi velocity is maximum and minimum, respectively. The Fermi velocity lies in-between the maxima and minima in the green regions.

(DOSs) for $LaNiO_2$ and $NdNiO_2$ in the non-magnetic (NM) phase, with the various orbital-resolved and site-resolved projections overlaid. In $LaNiO_2$, Fig. 2a, two distinct bands are seen crossing the Fermi level: one band is of nearly pure Ni-$3d_{x^2-y^2}$ character, while the other is derived from Ni ($3d_{z^2}$, $3d_{xy/yz}$) and La $5d$ orbitals. The latter band produces a spherical 3D electron-like Fermi surface at Γ and A symmetry points (Fig. 2c), whereas the former band generates a large, slightly warped quasi-2D cylindrical Fermi surface similar to the cuprates. These results are consistent with previous LDA[18], GGA[25], DFT+U[45], and LDA +DMFT[31] studies. Notably, the $3d_{x^2-y^2}$ band here bears a striking resemblance to the corresponding band in the cuprates[37], except that the position of the VHS here shifts from being below to above the Fermi level along the k_z direction in the Brillouin zone. As a result, the Fermi surface transitions from being open in the Γ plane ($k_z = 0$) to becoming closed in the Z plane ($k_z = \pi/c$) (Fig. 2c).

Figure 2b shows that the f electrons in $NdNiO_2$ lie close to the Fermi level while this is not the case in $LaNiO_2$. The Ni $3d$ dispersion in $LaNiO_2$ and $NdNiO_2$ is similar and this similarity persists across all the magnetic phases we have investigated (Figs. 3, 4, 5, 6). There is significant hybridization between the Nd $4f$ and Ni $3d$ orbitals which can give rise to self-doping effects and induce Kondo physics[24,26–28,30]. Regarding the Fermi surface

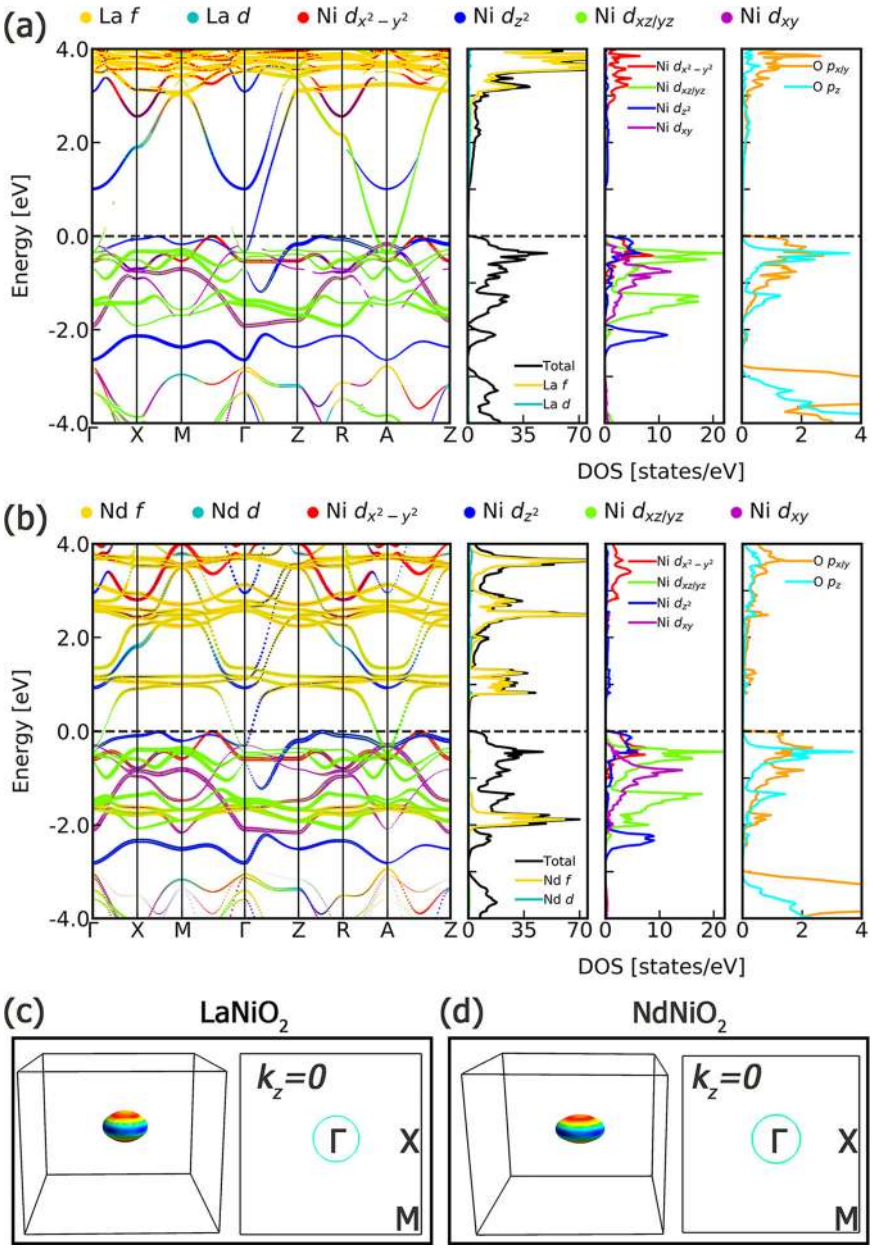

Fig. 4 The calculated electronic structures and Fermi surfaces of *G*-type antiferromagnetic (*G*-AFM) phase. Orbitally-projected electronic structures of the *G*-AFM phase of **a** $LaNiO_2$ and **b** $NdNiO_2$. Band structures are unfolded into the primitive $1\times1\times1$ Brillouin zone. **c** Fermi surface of $LaNiO_2$ and its projection of on the $k_z = 0$ plane. **d** Same as **c** but for $NdNiO_2$. Red and blue colors identify portions of the Fermi surface where the Fermi velocity is maximum and minimum, respectively. The Fermi velocity lies in-between the maxima and minima in the green regions.

in Fig. 2d, it is seen to display a double-goblet-like hole pocket along the Γ–Z direction with a narrow stem at Γ. Moreover, a large and complex hole Fermi surface appears surrounding Γ near the $k_z = 0$ plane, along with the formation of electron pockets near the *M* point. Note that in going from Γ to *Z* in the BZ, the goblet Fermi surface at the Γ point splits into the Fermi pockets around the *Z* point as the Fermi surface undergoes a change in topology (Fig. 2d).

Electronic structure of the C-AFM phase. Figures 3a, b present the unfolded electronic structure of $LaNiO_2$ and $NdNiO_2$ in the *C*-AFM phase. Like the cuprates, the *C*-AFM order is stabilized by the opening of a ~2 eV band gap in the $d_{x^2-y^2}$ band. However, unlike the cuprates, the 5*d* and 4*f* states fill the gap in the nickelates and maintain their metallic nature. In particular, the states near the Fermi level in $LaNiO_2$ mainly consist of Ni $3d_{z^2}$ and La 5*d* orbitals (Fig. 3a). Moreover, a flat band is seen pinned at the Fermi level along the $Z-R-A-Z$ line, originating from the Ni $3d_{z^2}$ orbitals. $NdNiO_2$ hosts a similar flat band, which also stems from Ni $3d_{z^2}$ bands. These flat band features have also been noted by Choi et al.[46], who used a large U to push the Nd 4*f* states away from the Fermi level. Flat bands produce highly anisotropic Fermi surfaces near the $k_z = \pi/c$ plane in both $LaNiO_2$ and $NdNiO_2$ (Figs. 3c, d). In $NdNiO_2$, there is one additional (ellipsoidal) electron pocket with good dispersion (Fig. 3d), which result from strong Nd 4*f*–Ni $3d_{z^2}$ hybridization.

Notably, the appearance of a flat band at the Fermi energy and the associated VHS can produce a landscape of nearly degenerate states[46]. Our calculations on a slightly distorted lattice (see

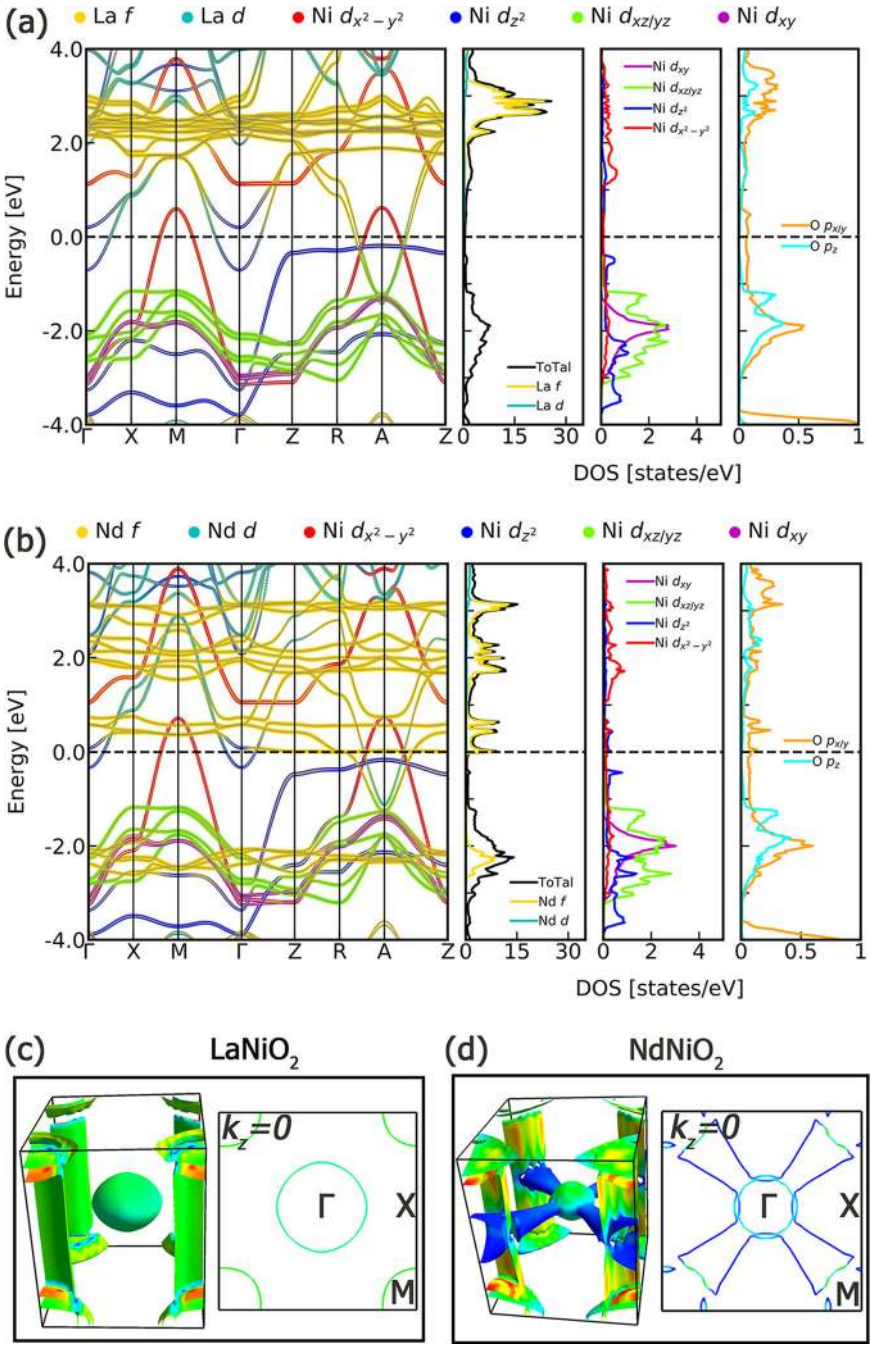

Fig. 5 The calculated electronic structures and Fermi surfaces of ferromagnetic (FM) phase. Orbitally-projected electronic structures of FM phase of **a** $LaNiO_2$ and **b** $NdNiO_2$. **c** The calculated Fermi surface of $LaNiO_2$ and the projection of the Fermi surface on $k_z = 0$ plane. **d** Same as **c** but for $NdNiO_2$. Red and blue colors identify portions of the Fermi surface where the Fermi velocity is maximum and minimum, respectively. The Fermi velocity lies in-between the maxima and minima in the green regions.

Supplementary Note 2 and Fig. S2) show that the distorted *C*-AFM phase is lower in energy by only ~3 meV/f.u. compared to the undistorted case. In this connection, we have also carried out computations on possible stripe phases in $NdNiO_2$ and, as expected, like the cuprates, we have found several low-energy stripe phases lying within 4–6 meV/f.u. of the ground state.

Electronic structure of the G-AFM phase. Figures 4a, b show the electronic structures of $LaNiO_2$ and $NdNiO_2$ in the *G*-AFM magnetic phase. This phase exhibits AFM coupling between the intralayer as well as the interlayer magnetic sites, which is to be contrasted with *C*-AFM where the interlayer coupling is FM. Interestingly, here we find no *f* bands near the Fermi level in $NdNiO_2$, so that the Fermi surfaces in $LaNiO_2$ and $NdNiO_2$ become similar. While the *G*-AFM and *C*-AFM phases are both dominated by the splitting of the $d_{x^2-y^2}$-band, and both phases host a region of suppressed DOS within ~0.7 eV of the Fermi level, these two phases differ in that a $3d_{z^2}$ band lies above the low DOS region in the *C*-AFM phase, but it lies below this DOS region in the *G*-AFM phase, resulting in a Fermi energy shift of ~0.7 eV between the two phases.

Electronic structure of the FM phase. Figures 5a, b present the electronic structure of $LaNiO_2$ and $NdNiO_2$ in the FM phase. As

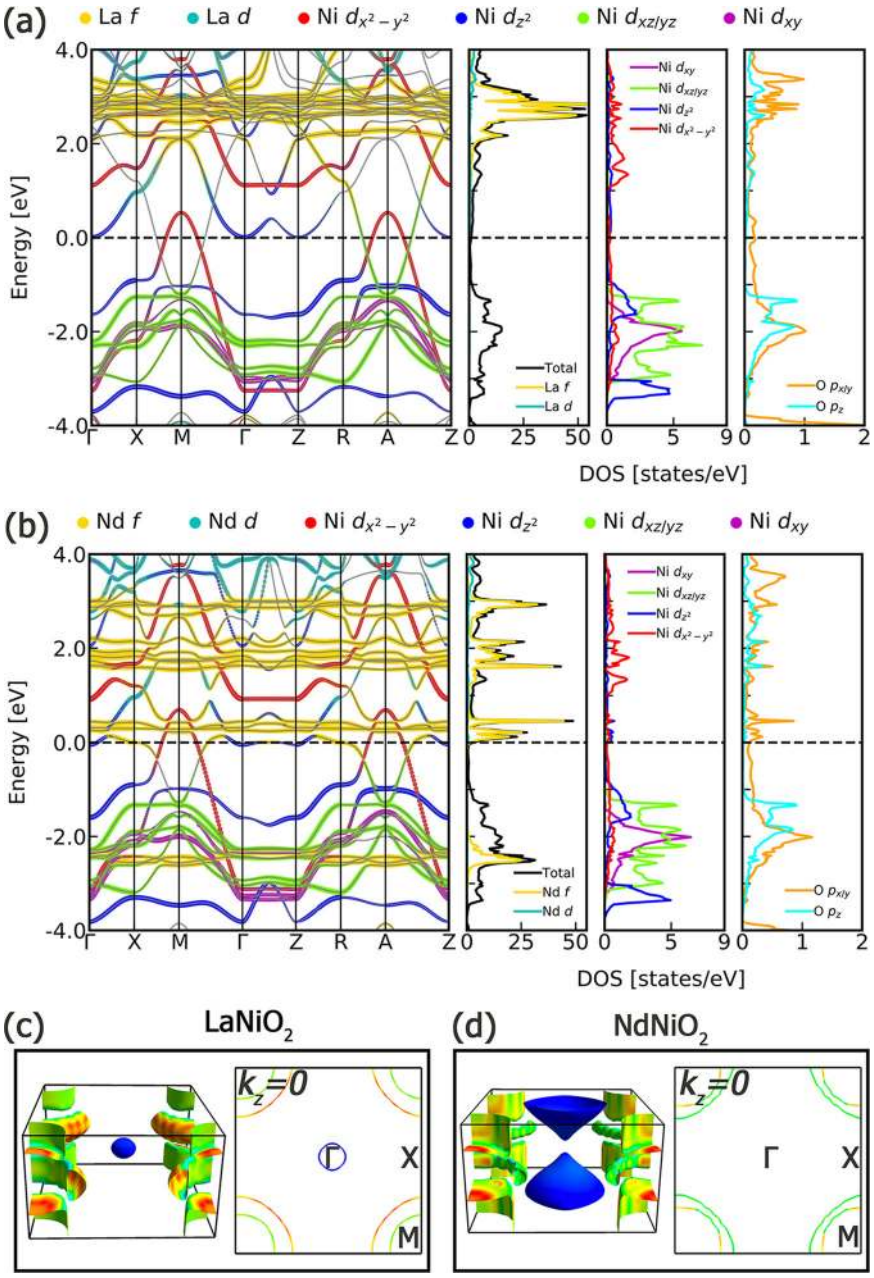

Fig. 6 The calculated electronic structures and Fermi surfaces of *A*-type antiferromagnetic (*A*-AFM) phase. Orbitally-projected electronic structures of the *A*-AFM phase of **a** $LaNiO_2$ and **b** $NdNiO_2$. Band structures are unfolded to the primitive $1 \times 1 \times 1$ Brillouin zone. **c** The calculated Fermi surface of $LaNiO_2$ and the projection of the Fermi surface on the $k_z = 0$ plane. **d** Same as **c** but for $NdNiO_2$. Red and blue colors identify portions of the Fermi surface where the Fermi velocity is maximum and minimum, respectively. The Fermi velocity lies in-between the maxima and minima in the green regions.

expected, the Ni $3d_{x^2-y^2}$ and $3d_{z^2}$ bands are now spin-split. The Fermi surface is composed of a Ni $3d_{x^2-y^2}$ hole pocket (red) at the M point and an electron pocket from the hybridization between the Ni $3d_{z^2}$ and Nd $4f$ orbitals at the Γ point (blue) (Fig. 5b). Interestingly, the majority spins in the Ni $3d_{x^2-y^2}$ and $3d_{z^2}$ bands point in opposite directions for a given Ni atom. Figures 5c, d show that the Fermi surfaces of $LaNiO_2$ and $NdNiO_2$ are quite similar, except that the Γ-point electron pocket in Fig. 5c has grown "propellers" in Fig. 5d, which is due to hybridization between the Ni $3d_{z^2}$ and Nd $4f$ orbitals. A 2D Fermi surface sheet centered at the M point is also seen extending in the k_z direction, produced by the hybridization of the Ni $3d_{xy/yz}$ and Nd $4f$ orbitals. Finally, there is an A-centered hole pocket generated by the Ni $3d_{x^2-y^2}$ band.

Electronic structure of the A-AFM phase. Figures 6a, b display the unfolded electronic band structure and DOSs of $LaNiO_2$ and $NdNiO_2$ in the *A*-AFM phase. Since the NiO_2 layers are ferromagnetically ordered, the band-splitting here is quite similar to that in the FM phase (Fig. 5). Figure 6a shows that the bands near the Fermi level in $LaNiO_2$ are mainly of Ni $3d_{x^2-y^2}$ and hybridized Ni $3d_{z^2}$-La $5d$ characters. However, in $NdNiO_2$, the main low-lying states near the Fermi level originate from Nd $4f$ states hybridizing with the Ni $3d_{x^2-y^2}$ and $3d_{z^2}$ orbitals. Notably, around -1 eV we see a strong mixing between the Ni $3d_{x^2-y^2}$ and $3d_{z^2}$ orbitals in both $LaNiO_2$ and $NdNiO_2$ along the $\Gamma - X$ and $R - A$ directions, which is absent in the NM and FM phases. This strong "orbital-mixing" effect could make the physics of the nickelates quite different from that of the cuprates.

Figures 6c, d show that the Fermi surfaces of $LaNiO_2$ and $NdNiO_2$ in the *A*-AFM phase fall into two categories: (1) The $M-A$ direction in both materials is similar to the corresponding FM Fermi surfaces, except for the splitting along the k_z direction due to the AFM stacking of the adjacent FM layers, which leads to the appearance of two pockets near the M point in the Γ-plane. And (2), the $\Gamma - Z$ direction is reminiscent of the NM case, with a Ni $3d_{z^2}$ electron pocket at the Γ point in $LaNiO_2$, while in $NdNiO_2$, the goblet Fermi surface of the NM phase is seen split into the Z-centered pockets. The blue color of these features (low Fermi velocity) suggests the presence of strong *f*-electron mixing.

Table 2 Comparison of properties of various phases of the nickelates and cuprates. Δ_{dp} and Δ_{e_g} denote the splitting of the metallic (Ni and Cu) 3*d* and O 2*p* bands, and the splitting of the transition-metal ions (Ni and Cu) e_g bands, respectively.

Phases	Δ_{dp} (eV)	Δ_{e_g} (eV)	*U* (eV)	J_H (eV)
$LaNiO_2$				
NM	3.21	1.93	-	-
FM	2.70	2.23	4.88	1.01
A-AFM	2.68	1.93	4.99	1.14
C-AFM	2.73	2.02	5.21	1.11
G-AFM	2.72	2.09	5.70	1.45
$NdNiO_2$				
NM	3.17	1.94	-	-
FM	2.19	2.04	5.08	1.23
A-AFM	2.31	2.00	4.99	2.14
C-AFM	2.39	2.11	5.27	1.00
G-AFM	2.69	2.13	5.78	1.94
$CaCuO_2$				
C-AFM	0.21	2.65	5.35	1.29
La_2CuO_4				
G-AFM	0.30	1.23	4.85[37]	1.25[37]

U and J_H denote effective on-site Hubbard potential and the Hund's coupling, respectively

***f*-electron dispersion**. Based on the preceding discussion of the electronic structures, we adduce that the various magnetic phases of $NdNiO_2$ are mainly stabilized by the Ni *d*-electrons, with the *f* electrons playing a minor role. The Fermi surfaces, however, are strongly affected by the Nd 4*f*-electrons through their strong mixing with the Ni 3*d* orbitals. The cluster of *f*-derived bands in the NM phase splits into three subbands once the Nd atoms become polarized, where the detailed structure of the bands depends on the magnetic order, much as is the case in our recent study of SmB_6[44].

Comparison with the cuprates. Table 2 gives the calculated $d-p$ splitting Δ_{dp}, Ni $d_{x^2-y^2} - d_{z^2}$ splitting Δ_{e_g}, Hubbard *U*, and Hund's coupling J_H values for the investigated magnetic phases of $LaNiO_2$ and $NdNiO_2$, along with the corresponding values for the cuprates. These quantities are defined precisely in the "Methods" section. Δ_{dp} for $LaNiO_2$ ranges from 2.68 (*A*-AFM) to 3.21 eV (NM), while in $NdNiO_2$, it spans 2.19–3.17 eV. The partial-DOSs for the Ni and Cu 3*d* and O 2*p* orbitals are shown in Figs. 7a, c, which refer to the *C*-AFM phase of $NdNiO_2$ and $CaCuO_2$, respectively. The O-2*p* band-center is seen to be lower than that of the Ni-3*d* bands by ~2 eV in $NdNiO_2$, but the O-2*p* levels are strongly hybridized with Cu $3d_{x^2-y^2}$ orbitals near the Fermi level in $CaCuO_2$. We estimate Δ_{dp} in $CaCuO_2$ in the *C*-AFM phase to be 0.19 eV, which is significantly smaller than its value in the nickelates. This is also the case for the single-layer La_2CuO_4 in the *G*-AFM phase, where we estimate Δ_{dp} to be 0.30 eV. These results suggest that $LaNiO_2$ and $NdNiO_2$ are closer to the Mott–Hubbard limit rather than being the charge-transfer case in the Zaanen–Sawatzky–Allen classification scheme[56].

For the NM state, our values of Δ_{dp} for $LaNiO_2$ and $NdNiO_2$ are 3.21 eV and 3.17 eV, respectively, which are smaller than the previously reported values of 4.4[18] and 3.7 eV[57]. Note, however, that we obtain Δ_{dp} directly from our first-principles results,

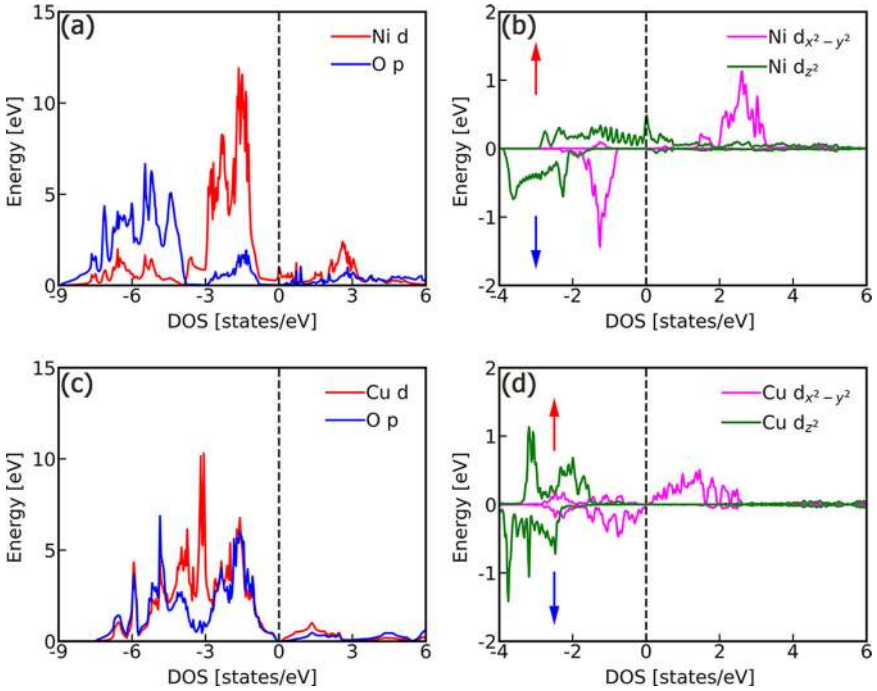

Fig. 7 Comparison the partial density of states (DOS) between *C*-type antiferromagnetic (*C*-AFM) phase of $NdNiO_2$ and $CaCuO_2$. a, **b** Partial DOSs for various sites and orbitals (see legend) in the *C*-AFM phase of $NdNiO_2$. **c**, **d** Same as **a**, **b**, except that these panels refer to the *C*-AFM phase of $CaCuO_2$.

Table 3 Estimated exchange interactions for the Ni sub-lattice in $LaNiO_2$ and $NdNiO_2$.

	$LaNiO_2$	$NdNiO_2$	La_2CuO_4
J_1 (meV)	52	118	138[37]
J_2 (meV)	−24	−74	-
J_3 (meV)	5	13.5	-

J_1 (intralayer nearest neighbor), J_2 (interlayer nearest neighbor), and J_3 (interlayer next-nearest neighbor) for $LaNiO_2$ and $NdNiO_2$. The in-plane J_1 for La_2CuO_4 is also listed for comparison.

which, as ref. [18] has pointed out, yield smaller values than those based on Wannier fitting of the band structure used by refs. [18,57]. For the magnetic phases, the values of Δ_{dp} are smaller than for the NM phase due to the wider d and p orbital spread.

Interestingly, values of Δ_{e_g} for the various magnetic phases of $LaNiO_2$ and $NdNiO_2$ are all about 2 eV. For example, the Δ_{e_g} for $LaNiO_2$ in the NM phase is 1.93 eV, which is close to the value of 1.95 eV reported in ref. [18]. The similarity of Δ_{e_g} values across the infinite-layer nickelates suggests that the Nd 4f electrons play a limited role in splitting the Ni 3d levels. Values of Δ_{e_g} for C-AFM $CaCuO_2$ and G-AFM La_2CuO_4 read from Figs. 7b, d are comparable to the values for the nickelates given in Table 2.

In order to ascertain the strength of electronic correlations on the nickel site, we have estimated the value of effective Hubbard U and Hund's coupling J_H in $LaNiO_2$ and $NdNiO_2$ for various magnetic arrangements using Eqs. (2, 3, 4), see "Methods" section below. Values of U so obtained for $LaNiO_2$, $NdNiO_2$, $CaCuO_2$, and La_2CuO_4 are similar, suggesting that the electronic correlations in all these materials are of similar strength. [Our estimated U values are consistent with other recent studies[24,57].] The behavior of J_H is more subtle. J_H values for the nickelates and cuprates are similar, although J_H for $NdNiO_2$ is larger in the A-AFM and G-AFM phases, indicating that J_H is sensitive to the effects of interlayer coupling.

Although the mechanism of superconductivity in the HTSCs remains controversial, the view that spin-fluctuations play a central role in determining the physical properties of the cuprates has been gaining increasing acceptance. In this scenario, the exchange-coupling strength would be a good descriptor for the robustness of superconductivity. Accordingly, we consider three different exchange interactions in the Ni sub-lattice: J_1 (intralayer nearest-neighbor), J_2 (interlayer nearest-neighbor), and J_3 (interlayer next-nearest-neighbor), which are shown in Fig. 1b. We estimated strengths of these exchange couplings by computing the total energies of various magnetic phases using the following Heisenberg Hamiltonian.

$$H = \frac{1}{2}\sum_{i,j} J_{i,j}\mathbf{S}_i\mathbf{S}_j, \quad (1)$$

where $S = \frac{1}{2}$. Here, $J > 0$ and $J < 0$ will represent the AFM and FM spin exchange interaction, respectively. Notably, Nomura et al.[58] have recently used an approach very similar to ours, where they obtain J in the nickelates by estimating its value in closely related insulating compounds. We have also used our technique in $YBCO_7$[38] and found the resulting J value to be in good agreement with RIXS experiments. For these reasons, we expect our approach for estimating J in the infinite-layer nickelates to be reasonable.

The calculated exchange parameters for $LaNiO_2$ and $NdNiO_2$ are listed in Table 3. The in-plane exchange coupling is seen to be antiferromagnetic where J_1 is the largest with a value of 52 meV in $LaNiO_2$ and 118 meV in $NdNiO_2$, which are comparable to the values based on a recent LDA+U calculation[49]. Interestingly,

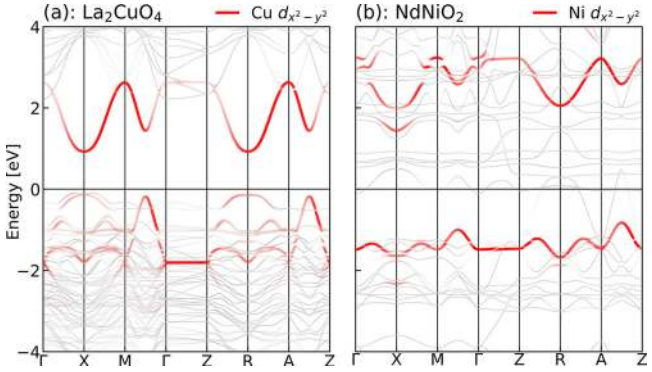

Fig. 8 Comparison the $3d_{x^2-y^2}$ band between G-type antiferromagnetic (G-AFM) phase of La_2CuO_4 and C-type antiferromagnetic (C-AFM) of $NdNiO_2$. a Cu $3d_{x^2-y^2}$ band for G-AFM La_2CuO_4. **b** Ni $3d_{x^2-y^2}$ band for C-AFM $NdNiO_2$. Band structures have been unfolded into the 1 × 1 × 1 primitive Brillouin zone.

the out-of-plane couplings show a competition between the ferromagnetic and antiferromagnetic orders. The larger J values in $NdNiO_2$ (compared to $LaNiO_2$) are due to its smaller lattice constant.

Superconductivity in the cuprates evolves out of a Mott insulator[3], whereas in the iron pnictides it emerges from a metallic state[59] with strong local magnetic fluctuations. Is magnetic order necessary for d-electron high-T_c superconductivity? The Ni-based superconductors appear to present a counter-example, although both Ni and Nd generally display significant magnetic moments with evidence of magnetic fluctuations or short-range order[32,46]. Notably, the undoped nickelates are not ordinary metals, but weak insulators[8,10]. In our previous SCAN-based studies of various correlated materials, we found many competing low-energy magnetic phases indicative of the presence of prominent magnetic fluctuations[37,38,44]. In the nickelates, our study of the various AFM orders finds a ~0.7 eV "pseudogap" (region of low DOS) near the Fermi level, which could explain their weak insulating behavior. Figure 8 compares the AFM gaps in the ground states of the cuprates (a) and the nickelates (b): The gap is seen to be about twice as large in the nickelates compared to the cuprates[37].

It is clear that there is a good deal of similarity between the cuprates and nickelates, both in the dispersion of the NM $d_{x^2-y^2}$ band and in the resulting magnetic orders, with the f electrons playing little role in the magnetic transitions even though f electrons modify the Fermi surfaces substantially. Although our normal-state DFT calculation cannot directly address superconductivity, our observation of competing AFM and FM exchange couplings in the nickelates may provide insight into why the T_c dome is smaller in the nickelates compared to the cuprates. Note that, Gu et al.[9] recently reported mixed s-gaps and d-gaps in scanning tunneling microscopy, while a theory paper by Wu et al.[60] suggested that the s-wave gap here is a surface effect due to a distorted top NiO_2 layer, which would of course not be captured in our bulk calculations. On the other hand, superconductivity has been found in two rare-earth substituted nickelates[7,21], but not in the parent La-based compound, suggesting a more significant role of f electrons. An interesting possibility is that the f electrons lead to heavy-fermion physics (flat bands), which is not present in the cuprates.

Conclusions. We present an in-depth examination of the role of f electrons and magnetic ordering effects in $LaNiO_2$ and $NdNiO_2$ within a parameter-free, all-electron first-principles framework.

The magnetic orders in the nickelates are found to be very similar to those in the cuprates in that the transitions are driven by the gapping of the $d_{x^2-y^2}$ band. Compared to the cuprates, the nickelates have a reduced J value with competing AFM and FM spin orders. While the 4f electrons play little role in the magnetism of the nickelates, they substantially modify Fermi surfaces in various magnetic states. Our analysis indicates that competing low-energy states could be driven in the nickelates via lattice distortions and stripe formation like the cuprates. Our study thus further reveals the importance of fluctuating magnetic order in correlated materials[38].

Methods

All calculations were performed by using the pseudopotential projector-augmented wave method[61] as implemented in the Vienna ab initio simulation package (VASP)[62,63]. A high-energy cutoff of 520 eV was used to truncate the plane-wave basis set. The exchange–correlation effects were treated using the SCAN[36] meta-GGA functional. Spin–orbit coupling effects were included self-consistently. The crystal structures and ionic positions were fully optimized using a force convergence criterion of 0.01 eV/Å for each atom along with a total energy tolerance of 10^{-5} eV. The Fermi surfaces were obtained with the FermiSurfer code[64]. The unfolded band structures including orbital characters were extracted from the supercell pseudo-wavefunction calculations[65] using the VaspBandUnfolding code[66].

In order to facilitate comparison with the cuprates, we calculated two quantities: (1) the charge-transfer energy between the Ni 3d and O 2p orbitals, $\Delta_{dp} = \varepsilon_d - \varepsilon_p$; and, (2) the energy-splitting between the two Ni e_g orbitals, $\Delta_{e_g} = \varepsilon_{x^2-y^2} - \varepsilon_{z^2}$. Here, ε_i refers to the band center of the ith orbital. Following previous work,[18,67] we defined band centers as, $\varepsilon_i = \frac{\int g_i(\varepsilon)\varepsilon d\varepsilon}{\int g_i(\varepsilon) d\varepsilon}$, where $g_i(\varepsilon)$ refers to the partial-density-of-states (PDOS) associated with orbital i. The integration range for Δ_{dp} is set to cover the full bonding and antibonding bands[67], whereas Δ_{e_g} is obtained from an integral over the antibonding bands alone, using an energy window of −3.5 to 2 eV and −4 to 4 eV for the NM and magnetic phases, respectively.

In order to estimate the effective on-site Hubbard potential U and the Hund's coupling J_H, we follow the method of Lane et al.[37]. Using the site-projected orbital-resolved PDOS $g_{\mu\sigma}$, we determine the average spin-splitting of the μ levels as follows:

$$\overline{E}_{\mu\sigma} = \int_W E g_{\mu\sigma}(E)\, \mathrm{d}E, \tag{2}$$

$$\overline{E}_{d_{x^2-y^2}\uparrow} - \overline{E}_{d_{x^2-y^2}\downarrow} = U(N_\uparrow - N_\downarrow), \tag{3}$$

$$\overline{E}_{\mu\neq d_{x^2-y^2}\uparrow} - \overline{E}_{\mu\neq d_{x^2-y^2}\downarrow} = J_H(N_\uparrow - N_\downarrow), \tag{4}$$

where $N_\uparrow$ ($N_\downarrow$) is the occupation of the spin-up (down) $d_{x^2-y^2}$ orbital and the integration is over the full bandwidth W.

Data availability

The data that support the findings of this study are available from the corresponding author upon reasonable request.

Received: 12 September 2020; Accepted: 7 May 2021;
Published online: 07 June 2021

References

1. Bednorz, J. G. & Müller, K. A. Possible high Tc superconductivity in the Ba-La-Cu-O system. *Z. Phys. B* **64**, 189–193 (1986).
2. Anderson, P. W. Physics: Is there glue in cuprate superconductors? *Science* **316**, 1705–1707 (2007).
3. Lee, P. A., Nagaosa, N. & Wen, X.-G. Doping a Mott insulator: physics of high-temperature superconductivity. *Rev. Mod. Phys.* **78**, 17–85 (2006).
4. Anderson, P. W. et al. The physics behind high-temperature superconducting cuprates: the plain vanilla version of RVB. *J. Phys.* **16**, R755–R769 (2004).
5. Norman, M. R. The challenge of unconventional superconductivity. *Science* **332**, 196–200 (2011).
6. Keimer, B., Kivelson, S. A., Norman, M. R., Uchida, S. & Zaanen, J. From quantum matter to high-temperature superconductivity in copper oxides. *Nature* **518**, 179–186 (2015).
7. Li, D. et al. Superconductivity in an infinite-layer nickelate. *Nature* **572**, 624–627 (2019).
8. Zeng, S. et al. Phase diagram and superconducting dome of infinite-layer $Nd_{1-x}Sr_xNiO_2$ thin films. *Phys. Rev. Lett.* **125**, 147003 (2020).
9. Gu, Q. et al. Single particle tunneling spectrum of superconducting $Nd_{1-x}Sr_xNiO_2$ thin films. *Nat. Commun.* **11**, 6027 (2020).
10. Li, D. et al. Superconducting dome in $Nd_{1-x}Sr_xNiO_2$ infinite layer films. *Phys. Rev. Lett.* **125**, 027001 (2020).
11. Wang, B.-X. et al. Synthesis and characterization of bulk $Nd_{1-x}Sr_xNiO_2$ and $Nd_{1-x}Sr_xNiO_3$. *Phys. Rev. Mater.* **4**, 084409 (2020).
12. Sawatzky, G. A. Superconductivity seen in a non-magnetic nickel oxide. *Nature* **572**, 592–593 (2019).
13. Norman, M. R. Entering the nickel age of superconductivity. *Physics* **13**, 85 (2020).
14. Wu, X. et al. Robust $d_{x^2-y^2}$-wave superconductivity of infinite-layer nickelates. *Phys. Rev. B* **101**, 060504 (2020).
15. Zhang, G.-M., Yang, Y.-f. & Zhang, F.-C. Self-doped Mott insulator for parent compounds of nickelate superconductors. *Phys. Rev. B* **101**, 020501 (2020).
16. Choi, M. Y., Lee, K. W. & Pickett, W. E. Role of 4f states in infinite-layer $NdNiO_2$. *Phys. Rev. B* **101**, 20503 (2020).
17. Jiang, M., Berciu, M. & Sawatzky, G. A. Critical nature of the Ni spin state in doped $NdNiO_2$. *Phys. Rev. Lett.* **124**, 207004 (2020).
18. Botana, A. S. & Norman, M. R. Similarities and differences between $NdNiO_2$ and $CaCuO_2$ and implications for superconductivity. *Phys. Rev. X* **10**, 011024 (2020).
19. Karp, J. et al. Many-body electronic structure of $NdNiO_2$ and $CaCuO_2$. *Phys. Rev. X* **10**, 021061 (2020).
20. Li, Q. et al. Absence of superconductivity in bulk $Nd_{1-x}Sr_xNiO_2$. *Commun. Mater.* **1**, 16 (2020).
21. Osada, M. et al. A superconducting praseodymium nickelate with infinite layer structure. *Nano Lett.* **20**, 5735–5740 (2020).
22. Hayward, M. & Rosseinsky, M. Synthesis of the infinite layer Ni(I) phase $NdNiO_{2+x}$ by low temperature reduction of $NdNiO_3$ with sodium hydride. *Solid State Sci.* **5**, 839–850 (2003).
23. Hayward, M. A., Green, M. A., Rosseinsky, M. J. & Sloan, J. Sodium hydride as a powerful reducing agent for topotactic oxide deintercalation: synthesis and characterization of the nickel(I) oxide $LaNiO_2$. *J. Am. Chem. Soc.* **121**, 8843–8854 (1999).
24. Nomura, Y. et al. Formation of a two-dimensional single-component correlated electron system and band engineering in the nickelate superconductor $NdNiO_2$. *Phys. Rev. B* **100**, 205138 (2019).
25. Jiang, P., Si, L., Liao, Z. & Zhong, Z. Electronic structure of rare-earth infinite-layer $RNiO_2$ (R = La, Nd). *Phys. Rev. B* **100**, 201106 (2019).
26. Zhang, H. et al. Effective Hamiltonian for nickelate oxides $Nd_{1-x}Sr_xNiO_2$. *Phys. Rev. Res.* **2**, 013214 (2020).
27. Gu, Y., Zhu, S., Wang, X., Hu, J. & Chen, H. A substantial hybridization between correlated Ni-d orbital and itinerant electrons in infinite-layer nickelates. *Commun. Phys.* **3**, 84 (2020).
28. Liu, Z., Ren, Z., Zhu, W., Wang, Z. & Yang, J. Electronic and magnetic structure of infinite-layer $NdNiO_2$: trace of antiferromagnetic metal. *npj Quantum Mater.* **5**, 31 (2020).
29. Olevano, V., Bernardini, F., Blase, X. & Cano, A. Ab initio many-body GW correlations in the electronic structure of $LaNiO_2$. *Phys. Rev. B* **101**, 161102 (2020).
30. Lechermann, F. Late transition metal oxides with infinite-layer structure: nickelates versus cuprates. *Phys. Rev. B* **101**, 081110 (2020).
31. Ryee, S., Yoon, H., Kim, T. J., Jeong, M. Y. & Han, M. J. Induced magnetic two-dimensionality by hole doping in the superconducting infinite-layer nickelate $Nd_{1-x}Sr_xNiO_2$. *Phys. Rev. B* **101**, 064513 (2020).
32. Leonov, I., Skornyakov, S. L. & Savrasov, S. Y. Lifshitz transition and frustration of magnetic moments in infinite-layer $NdNiO_2$ upon hole doping. *Phys. Rev. B* **101**, 241108 (2020).
33. Hu, L.-H. & Wu, C. Two-band model for magnetism and superconductivity in nickelates. *Phys. Rev. Res.* **1**, 1–5 (2019).
34. Hepting, M. et al. Electronic structure of the parent compound of superconducting infinite-layer nickelates. *Nat. Mater.* **19**, 381–385 (2020).
35. Pokharel, K. et al. Ab intio description of the electronic structure of high-temperature cuprate superconductors: a comparative density functional study. *arXiv e-prints*https://arxiv.org/abs/2004.08047 (2020).
36. Sun, J., Ruzsinszky, A. & Perdew, J. Strongly constrained and appropriately normed semilocal density functional. *Phys. Rev. Lett.* **115**, 036402 (2015).
37. Lane, C. et al. Antiferromagnetic ground state of La_2CuO_4: a parameter-free ab initio description. *Phys. Rev. B* **98**, 125140 (2018).
38. Zhang, Y. et al. Competing stripe and magnetic phases in the cuprates from first principles. *Proc. Natl Acad. Sci.* **117**, 68–72 (2020).
39. Furness, J. W. et al. An accurate first-principles treatment of doping-dependent electronic structure of high-temperature cuprate superconductors. *Commun. Phys.* **1**, 11 (2018).
40. Nokelainen, J. et al. Ab initio description of the $Bi_2Sr_2CaCu_2O_{8+\delta}$ electronic structure. *Phys. Rev. B* **101**, 1–8 (2020).

41. Lane, C. & Zhu, J. X. Landscape of coexisting excitonic states in the insulating single-layer cuprates and nickelates. *Phys. Rev. B* **101**, 1–10 (2020).
42. Lane, C. et al. First-principles calculation of spin and orbital contributions to magnetically ordered moments in Sr_2IrO_4. *Phys. Rev. B* **101**, 155110 (2020).
43. Varignon, J., Bibes, M. & Zunger, A. Mott gapping in 3*d* ABO_3 perovskites without Mott-Hubbard interelectronic repulsion energy *U*. *Phys. Rev. B* **100**, 035119 (2019).
44. Zhang, R. et al. Understanding the Quantum oscillation spectrum of heavy-fermion compound SmB_6. *arXiv e-prints* https://arxiv.org/abs/2003.11052 (2020).
45. Lee, K. W. & Pickett, W. E. Infinite-layer $LaNiO_2$: Ni^{1+} is not Cu^{2+}. *Phys. Rev. B* **70**, 1–7 (2004).
46. Choi, M.-Y., Pickett, W. E. & Lee, K.-W. Fluctuation-frustrated flat band instabilities in $NdNiO_2$. *Phys. Rev. Res.* **2**, 033445 (2020).
47. Chang, J., Zhao, J. & Ding, Y. Hund-heisenberg model in superconducting infinite-layer nickelates. *Eur. Phys. J. B* **93**, 1–7 (2020).
48. Kitatani, M. et al. Nickelate superconductors-a renaissance of the one-band Hubbard model. *npj Quantum Mater.* **5**, 59 (2020).
49. Wan, X., Ivanov, V., Resta, G., Leonov, I. & Savrasov, S. Y. Exchange interactions and sensitivity of the Ni two-hole spin state to Hund's coupling in doped $NdNiO_2$. *Phys. Rev. B* **103**, 075123 (2021).
50. Fu, Y. et al. Core-level x-ray photoemission and Raman spectroscopy studies on electronic structures in Mott-Hubbard type nickelate oxide $NdNiO_2$. *arXiv e-prints*https://arxiv.org/abs/1911.03177 (2019).
51. Cui, Y. et al. NMR evidence of antiferromagnetism in $Nd_{0.85}Sr_{0.15}NiO_2$. *arXiv e-prints*https://arxiv.org/abs/2011.09610 (2020).
52. Liu, C. et al. Observation of an antiferromagnetic quantum critical point in high-purity $LaNiO_3$. *Nat. Commun.* **11**, 1402 (2020).
53. Zhang, Y. et al. Symmetry-breaking polymorphous descriptions for correlated materials without interelectronic *U*. *Phys. Rev. B* **102**, 045112 (2020).
54. Wang, Z., Zhao, X.-G., Koch, R., Billinge, S. J. L. & Zunger, A. Understanding electronic peculiarities in tetragonal fese as local structural symmetry breaking. *Phys. Rev. B* **102**, 235121 (2020).
55. Perdew, J. P., Ruzsinszky, A., Sun, J., Nepal, N. K. & Kaplan, A. D. Interpretations of ground-state symmetry breaking and strong correlation in wavefunction and density functional theories. *Proc. Natl Acad. Sci.* **118**, e2017850118 (2021).
56. Zaanen, J., Sawatzky, G. A. & Allen, J. W. Band gaps and electronic structure of transition-metal compounds. *Phys. Rev. Lett.* **55**, 418–421 (1985).
57. Sakakibara, H. et al. Model construction and a possibility of cupratelike pairing in a new d^9 nickelate superconductor (Nd, Sr)NiO_2. *Phys. Rev. Lett.* **125**, 077003 (2020).
58. Nomura, Y., Nomoto, T., Hirayama, M. & Arita, R. Magnetic exchange coupling in cuprate-analog d^9 nickelates. *Phys. Rev. Res.* **2**, 043144 (2020).
59. Norman, M. High-temperature superconductivity in the iron pnictides. *Physics* **1**, 21 (2008).
60. Wu, X. et al. Surface *s*-wave superconductivity for oxide-terminated infinite-layer nickelates. *arXiv e-prints* https://arxiv.org/abs/2008.06009 (2020).
61. Kresse, G. & Joubert, D. From ultrasoft pseudopotentials to the projector augmented-wave method. *Phys. Rev. B* **59**, 1758–1775 (1999).
62. Kresse, G. & Hafner, J. Ab initio molecular dynamics for open-shell transition metals. *Phys. Rev. B* **48**, 13115–13118 (1993).
63. Kresse, G. & Furthmüller, J. Efficient iterative schemes for ab initio total-energy calculations using a plane-wave basis set. *Phys. Rev. B* **54**, 11169–11186 (1996).
64. Kawamura, M. FermiSurfer: Fermi-surface viewer providing multiple representation schemes. *Comput. Phys. Commun.* **239**, 197–203 (2019).
65. Popescu, V. & Zunger, A. Extracting *E* versus $\vec{k}$ effective band structure from supercell calculations on alloys and impurities. *Phys. Rev. B* **85**, 085201 (2012).
66. Zheng, Q. VaspBandUnfolding. https://github.com/QijingZheng/VaspBandUnfolding
67. Jang, S. W., Kotani, T., Kino, H., Kuroki, K. & Han, M. J. Quasiparticle self-consistent *GW* study of cuprates: electronic structure, model parameters and the two-band theory for T_c. *Sci. Rep.* **5**, 12050 (2015).
68. Kaneko, D., Yamagishi, K., Tsukada, A., Manabe, T. & Naito, M. Synthesis of infinite-layer $LaNiO_2$ films by metal organic decomposition. *Phys. C* **469**, 936–939 (2009).

Acknowledgements

The work at Tulane University was supported by the start-up funding from Tulane University, the Cypress Computational Cluster at Tulane, the Extreme Science and Engineering Discovery Environment (XSEDE), the DOE Energy Frontier Research Center (development and applications of density functional theory): Center for the Computational Design of Functional Layered Materials (DE-SC0012575), the DOE, Office of Science, Basic Energy Sciences Grant DE-SC0019350, and the National Energy Research Scientific Computing Center. The work at Northeastern University was supported by the U.S. DOE, Office of Science, Basic Energy Sciences grant number DE-FG02-07ER46352 and benefited from Northeastern University's Advanced Scientific Computation Center, the National Energy Research Scientific Computing Center supercomputing center (DOE grant number DEAC02-05CH11231). The work at Los Alamos National Laboratory was supported by the U.S. DOE NNSA under Contract No.89233218CNA000001 and by the Center for Integrated Nanotechnologies, a DOE BES user facility, in partnership with the LANL Institutional Computing Program for computational resources, the LDRD program. B.B. acknowledges support from the COST Action CA16218. The work at TIFR Mumbi was supported by the Department of Atomic Energy of the Government of India under projetct number 12-R&D-TFR-5.10-0100.

Author contributions

R.Z., C.L., B.S., and J.N. performed computations and analyzed the data. B.B., R.S.M., A.B., and J.S. led the investigations, designed the computational approaches, provided computational infrastructure and analyzed the results. All authors contributed to the writing of the manuscript.

Competing interests

The authors declare no competing interests.

Additional information

Supplementary information The online version contains supplementary material available at https://doi.org/10.1038/s42005-021-00621-4.

Correspondence and requests for materials should be addressed to R.Z., A.B. or J.S.

Reprints and permission information is available at http://www.nature.com/reprints

Publisher's note Springer Nature remains neutral with regard to jurisdictional claims in published maps and institutional affiliations.